



HAL
open science

Characterization of the viscoelastic properties of in vitro crystalline lens samples using ultrasound elastography

A. Ganeau, M. Lafond, F. Legrand, G. Laloy-Borgna, O. Ben Moussa, S. Poinard, F. Mascarelli, Gilles Thuret, P. Gain, C. Lafon, et al.

► To cite this version:

A. Ganeau, M. Lafond, F. Legrand, G. Laloy-Borgna, O. Ben Moussa, et al.. Characterization of the viscoelastic properties of in vitro crystalline lens samples using ultrasound elastography. Applied Physics Letters, 2023, 123 (10), pp.103701. 10.1063/5.0165197 . inserm-04355641

HAL Id: inserm-04355641

<https://inserm.hal.science/inserm-04355641v1>

Submitted on 20 Dec 2023

HAL is a multi-disciplinary open access archive for the deposit and dissemination of scientific research documents, whether they are published or not. The documents may come from teaching and research institutions in France or abroad, or from public or private research centers.

L'archive ouverte pluridisciplinaire **HAL**, est destinée au dépôt et à la diffusion de documents scientifiques de niveau recherche, publiés ou non, émanant des établissements d'enseignement et de recherche français ou étrangers, des laboratoires publics ou privés.



HAL
open science

Characterization of the viscoelastic properties of in vitro crystalline lens samples using ultrasound elastography

A. Ganeau, M. Lafond, F. Legrand, G. Laloy-Borgna, O. Ben Moussa, S. Poinard, F. Mascarelli, Gilles Thuret, P. Gain, C. Lafon, et al.

► To cite this version:

A. Ganeau, M. Lafond, F. Legrand, G. Laloy-Borgna, O. Ben Moussa, et al.. Characterization of the viscoelastic properties of in vitro crystalline lens samples using ultrasound elastography. Applied Physics Letters, 2023, 123 (10), 10.1063/5.0165197 . inserm-04355641

HAL Id: inserm-04355641

<https://inserm.hal.science/inserm-04355641>

Submitted on 20 Dec 2023

HAL is a multi-disciplinary open access archive for the deposit and dissemination of scientific research documents, whether they are published or not. The documents may come from teaching and research institutions in France or abroad, or from public or private research centers.

L'archive ouverte pluridisciplinaire **HAL**, est destinée au dépôt et à la diffusion de documents scientifiques de niveau recherche, publiés ou non, émanant des établissements d'enseignement et de recherche français ou étrangers, des laboratoires publics ou privés.

Characterization of the viscoelastic properties of *in vitro* crystalline lens samples using ultrasound elastography

A. Ganeau,¹ M. Lafond,^{1*} F. Legrand,¹ G. Laloy-Borgna,¹ O. Ben Moussa,² S. Poinard,² F. Mascarelli,^{2,3} G. Thuret,² P. Gain,² C. Lafon,¹ and S. Catheline¹

¹LabTAU, INSERM, Centre Léon Bérard, Université Lyon 1, Univ Lyon, F-69003, LYON, France

²Laboratoire de Biologie, Ingénierie et Imagerie pour l'Ophtalmologie (BiiO), Université Jean Monnet, SAINT-ETIENNE, France

³Centre de Recherche des Cordeliers, INSERM, PARIS, France

* maxime.lafond@inserm.fr

1 With aging, the stiffening of the crystalline lens^{1,2} can hinder accommodation and reduce near-
2 vision in more than, 75% of individuals above 40 year old³, an impairment known as presbyopia.
3 Mapping lens elasticity using shear wave elastography holds significant promise for monitoring
4 potential treatments for presbyopia. However, because of the transparency of the lens to
5 ultrasound, the tracking of waves can be performed only on its boundaries. The goal of this study
6 is to characterize the viscoelastic properties of *in vitro* crystalline lens samples with a curvilinear
7 harmonic method based on noise correlation algorithms. This procedure consists of precise
8 measurements of the dispersion of surface waves across a large frequency range (0.1–3.5 kHz),
9 thus allowing for clear identification of the wave properties needed to correctly estimate the
10 elasticity. The proposed method was applied to gelatin phantoms and excised porcine lens
11 samples. This enabled the observation of two regions in the dispersion curves: a sharp decrease in
12 dispersion at low frequencies (< 1 kHz), which was partly due to guided waves, and a smoother
13 slope at high frequencies (> 1 kHz), which was attributed to viscoelastic dispersion. In contrast to
14 previous studies, shear elasticity and viscosity moduli were computed at higher frequencies with
15 a Kelvin–Voigt model. If our approach confirms the shear viscosity of lenses, then the shear elastic
16 moduli of lenses are almost an order of magnitude greater than the results of previous studies.

17

18 Presbyopia, the most common vision impairment, affected approximately 1.8 billion people
19 worldwide in 2015³. It progressively degrades near vision primarily as the aging of the crystalline lens
20 decreases its deformability, as evidenced by a lens-spinning method^{2,4,5}. Compression tests and
21 dynamic mechanical analysis revealed increases in both the shear modulus and viscosity in aging lens<sup>6–
22 8</sup>. Studies using microindentors revealed an elasticity gradient in the lens, with the center being stiffer
23 than the cortex^{1,9,10}. The only noninvasive method suitable for clinical use is Brillouin spectroscopy,
24 which requires only incident light and enables local *in vivo* measurements of the compressional wave
25 speed c_L in the lenses of human patients^{11–13}. The c_L is related to both the longitudinal and shear

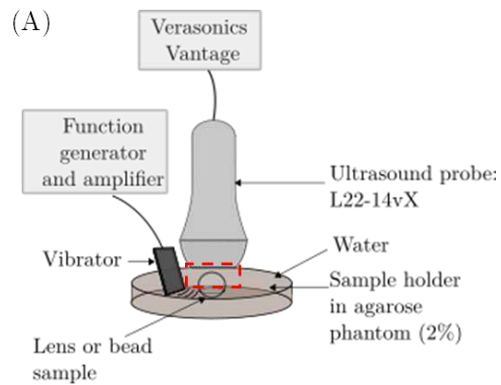
26 moduli. However, in soft biological tissues, the shear modulus is three orders of magnitude smaller
27 than the longitudinal modulus. Although both moduli are typically correlated in biological systems,
28 Brillouin spectroscopy alone does not allow for quantitative measurements of Young's modulus¹⁴.
29 Elastography allows noninvasive mapping of the shear modulus. However, speckle tracking methods
30 are not directly applicable in the lens because of its transparency to ultrasound and light. To overcome
31 this challenge, some teams chose to create artificial speckles in the form of laser-induced
32 microbubbles¹⁵⁻¹⁷. Young's moduli were calculated from the maximum displacement of the bubbles,
33 created by acoustic radiation force impulse (ARFI) and its relaxation time. Other groups chose to focus
34 on the only available backscattered signal from the interface of the lens. Displacement was induced by
35 ARFI and tracked by ultrasound imaging or optical coherence tomography (OCT). The same type of
36 computation was performed^{18,19}, and wave speeds were measured by time of flight^{18,20-22}. The shear
37 elasticity and viscosity moduli were deduced by assuming the nature of waves propagating in the
38 lens²³. Rayleigh or Scholte waves are usually used to describe surface waves, depending on the
39 boundary conditions. However, it is essential to consider the excitation frequency for small objects,
40 which is often overlooked.

41 Here, we present a method to analyze lens elasticity *in vitro*. Based on noise correlation algorithms,
42 this method performs harmonic curvilinear analysis of surface waves, studying their speed across a
43 large frequency range. This method identifies dispersive phenomena, aiding in the identification of
44 wave propagation regimes. It was applied to numerical simulations and experimental models, including
45 flat gelatin phantoms and beads. Finally, we conducted *in vitro* studies on young porcine lenses.

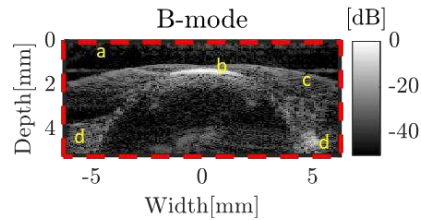
46

47 The setup included a mechanical vibrator (APA100M, Cedrat Technologies) in contact with a
48 1.3 cm thick, 6 cm diameter agarose gel sample holder (2% w/v). The holder had a hollow inclusion at
49 its center (Figure 1A). A function generator (Keysight Technologies) emitted a 0.1-3.5 kHz sweep of 400
50 ms at 3.5 Vpp. The signal was amplified by 20 dB (LC75B, LA75A, Cedrat Technologies) and delivered
51 to the vibrator. A 128-element linear imaging array centered at 15 MHz (L22-14vX, Vermon) was
52 positioned above the sample and connected to an ultrasound scanner (Vantage, Verasonics). The
53 acquisition of 4500 plane wave images was performed at a frame rate of 9000 fps. Figure 1B shows the
54 B-mode image of a lens sample embedded in the agarose holder, revealing artifacts from
55 backscattering interfaces. Implementing plane wave compounding could enhance image quality²⁴.
56 However, scanner limitations prevented simultaneous implementation of compounded imaging and a
57 high frame rate. Further investigation is needed to evaluate potential artifact-induced errors. The
58 excitation bandwidth was chosen close to the Shannon limit of 4.5 kHz, allowing for investigation of
59 multiple wave regimes. The vibrator was in contact with the agarose phantom adjacent to the sample,
60 enabling propagation of transverse waves along the lens interface, which was imaged by the

61 ultrasound probe. Three sample types were: flat gelatin phantom of 10% (w/v) and 15% (w/v)
 62 (thickness: 1.5–1.8 cm, diameter: 6 cm); 10% and 15% gelatin beads (1 cm diameter); and 11 lenses
 63 excised from 6-month-old pigs. Their maximum thickness was measured by ultrasound-imaging
 64 approximately to 7.51 ± 0.56 mm, which is very close to the study of I.Sanchez et al.²⁵. A 2% agarose
 65 gel was poured around the sample for optimal mechanical coupling, with ultrasound coupling provided
 66 by an iso-osmotic organoculture medium for lenses (CorneaMax®, EurobioSientific).



(B) a) Water b) Anterior interface
 c) Diffraction artefact
 d) Agarose phantom



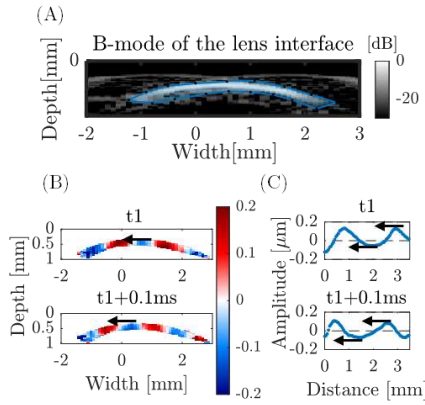
67
 68 FIG. 1. (A): Experimental setup: vibrator-induced displacements in the agarose sample holder and
 69 sample. A linear array connected to an ultrafast scanner was immersed in water during data
 70 acquisition. (B): B-mode image of the lens sample in the agarose phantom.

71

72 Figure 1B shows a representative ultrasound image of a lens embedded in the agarose sample holder,
 73 revealing the transparency of the lens except on its anterior interface where the waves were tracked.
 74 To test our method, a finite difference simulation of the 2-D elastic wave equation in the time domain
 75 was conducted. The simulation involved a homogenous soft solid with 0.8 cm diameter ($c_1=4$ m/s,

76 $\rho=1000 \text{ kg/m}^3$, viscosity $\mu_2=0.6 \text{ Pa}\cdot\text{s}$) embedded in “quasi water” ($c_1=0.001 \text{ m/s}$). An unrealistically low
 77 Poisson's ratio of 0.4 was chosen to prevent instability issues in the simulation. The purpose of this
 78 simulation was to assess the ability of the algorithm to extract the wave speed from surface waves.
 79 The simulation parameters included a 600 Hz source at the surface in a 251x251 grid with a sampling
 80 of $80 \mu\text{m}$ and time steps of $2.5 \mu\text{s}$.

81 Induced displacements on the sample surface (Figure 2A) were reconstructed using a phase
 82 tracking algorithm calculating the phase variation between two successive frames²⁶ (Figure 2B). Points
 83 were selected along a curvilinear line for lenses, gelatin beads, and the simulated inclusion. For flat
 84 phantoms, a straight line was chosen corresponding to the middle of the normal to both interface
 85 contours. The abscissa, whether curvilinear or linear, was calculated for each point. Interpolation was
 86 applied to ensure constant intervals between points, resulting in a vector of displacements (Figure 2C).
 87
 88



89
 90 FIG. 2. (A) B-mode of ultrasound scattering at the anterior interface of the lens. The blue area
 91 represents the tracked region. (B) Two successive displacement snapshots; wave fronts were observed
 92 on the interface. (C) Two successive snapshots of the curvilinear displacement field after 1D post-
 93 processing. Black arrows indicate the propagation direction.

94
 95 Analysis of the displacement field was based on a noise correlation algorithm^{27,28}. The main principle
 96 was to compute the time-reversed field ψ^{TR} of the displacement field ϕ , which was directly related to
 97 the cross-correlation function of ϕ :

98
$$\psi^{TR}(\vec{r}, t) = \phi(\vec{r}_0, t) \otimes_t \phi(\vec{r}_0 - \vec{r}, -t), \quad (1)$$

99 where \vec{r}_0 , \vec{r} are the location of the receiver point and the distance between the source and this
 100 receiver, respectively, and \otimes_t represents the time convolution product.

101 Figures 2B and 2C demonstrate that the displacement field was directionally oriented along the
 102 interface. Notably, the correlation algorithm was not biased by plane waves²⁹.

103 The wavelength λ can be calculated from the time-reversed field. For a monochromatic plane wave,
 104 $\phi(r, t) = Ae^{ikr} e^{i\omega t}$. Thus, the time-reversed field can be written as:

$$105 \quad \psi^{TR}(r, -t) = A^2 \overline{\psi^{TR}(r, -t)}, \quad (2)$$

106 with $\overline{\psi^{TR}(r, -t)} = e^{ikr} e^{i\omega t}$, the normalized time-reversed field.

107 Similarly, the second derivative of ψ^{TR} can be written as:

$$108 \quad \frac{\partial^2 \psi^{TR}(r, 0)}{\partial r^2} = -k^2 \psi^{TR}(r, 0),$$

$$109 \quad \Leftrightarrow \frac{\partial^2 \psi^{TR}(r, 0)}{\partial r^2} \times \frac{1}{\psi^{TR}(r, 0)} = -k^2, \quad (3)$$

$$110 \quad \Leftrightarrow \frac{\partial^2 A^2 \overline{\psi^{TR}(r, 0)}}{\partial r^2} \times \frac{1}{A^2 \overline{\psi^{TR}(r, 0)}} = \frac{-4\pi^2}{\lambda^2},$$

$$111 \quad \Leftrightarrow \frac{\partial^2 \overline{\psi^{TR}(r, 0)}}{\partial r^2} \times \frac{1}{\overline{\psi^{TR}(r, 0)}} = \frac{-4\pi^2}{\lambda^2}.$$

112 To obtain λ , we computed the previous equation at the source, $r = 0$:

$$113 \quad \lambda^2 = -4\pi^2 \left(\frac{\partial^2 \overline{\psi^{TR}(0,0)}}{\partial r^2} \right)^{-1}. \quad (4)$$

114 The wavelength was calculated by analyzing the phase of the time-reversed field. In practice, fast
 115 Fourier transform of the displacement vector was used, followed by independent cross-correlation of
 116 each monochromatic signal. In the Fourier domain, the time-reversed field can be written as:

$$117 \quad \overline{\psi^{TR}(\omega)} = \mathcal{R}e \left\{ TF(\overline{\psi^{TR}(r, t)}) \right\}. \quad (5)$$

118 In this study, $\overline{\psi^{TR}(\omega)}$ is called the correlation spectroscopy. Similarly, the wavelength can be retrieved
 119 from the curvature of the correlation spectroscopy:

$$120 \quad \lambda^2(\omega) = -4\pi^2 \left(\frac{\partial^2 \overline{\psi^{TR}(\omega)}}{\partial r^2} \right)^{-1}. \quad (6)$$

121 The correlation spectroscopy was spatially averaged, considering the distance between points along
 122 the interface. A sliding window of 10 Hz was used for averaging. Figure 3A shows the correlation
 123 spectroscopy of the 1D displacement along the flat interface of a 2% agarose phantom. It represents
 124 the spatial correlation of the displacement field in relation to frequency. The second derivative of the
 125 spatial correlation reveals the wavelength-frequency relationship (Eq. 6), indicating a decrease in
 126 wavelength with increasing frequency. To quantitatively study the dispersion of the medium, the
 127

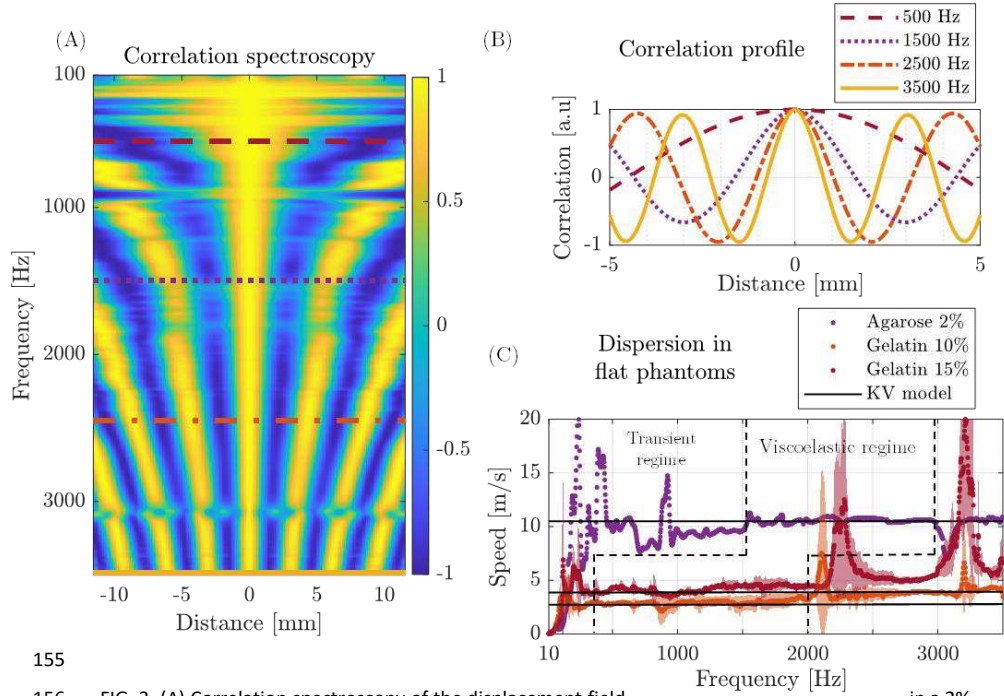
128 wavelength was derived from the correlation spectroscopy matrix by computing the curvature of the
129 correlation profile. The second derivative of the spatial correlation was numerically calculated:
130 $f''(x) = (f(x + \delta x) + f(x - \delta x) - 2f(x)) / \delta x^2$, where f is the function to differentiate, and
131 δx is the maximum derivative step corresponding to the full width at half maximum. Figure 3B shows
132 correlation profiles at four frequencies. The speed was computed at each frequency by the relationship
133 $c = \lambda \cdot \nu$, where ν is the frequency.

134 For waves of different natures, a rheological model can be selected to determine the elastic moduli. In
135 a purely elastic, isotropic and infinite solid, shear waves are nondispersive, and their speed depends
136 on only the density ρ and the shear modulus μ given by the relationship $c = \sqrt{(\mu/\rho)}$. In viscoelastic
137 solids, the Kelvin–Voigt model incorporates the viscosity term, resulting in a frequency-dependent
138 change in the speed of shear wave (c_T)³⁰ and rewritten as follows:

139
$$c_T(\omega) = \frac{\sqrt{2(\mu_1^2 + \omega^2 \mu_2^2)}}{\sqrt{\rho(\mu_1 + \sqrt{\mu_1^2 + \omega^2 \mu_2^2})}}. \quad (7)$$

140 The Kelvin–Voigt method is suitable for biological tissue³¹ and has been used in a study on the lens²³.
141 In our experiment, the waves can be approximated as Scholte waves due to the presence of the fluid-
142 medium boundary. The speed of these waves, denoted as c_{sh} , is proportional to the shear wave speed
143 and can be estimated as $c_{sh} \approx 0.84c_T$ ³². By substituting c_T with Equation (7), the modified rheological
144 model for Scholte waves is obtained. Waves can be guided within a solid structure, and in the case of
145 guided waves, the speed depends on both the elasticity term μ_1 and the waveguide thickness.

146
147
148
149
150
151
152
153
154



155
 156 FIG. 3. (A) Correlation spectroscopy of the displacement field
 157 agarose phantom: spatial correlation as a function of the frequency. (B) Correlation profile at multiple
 158 frequencies in a 2% agarose phantom. (C) Dispersion curves of the 2% agarose, 10% gelatin and 15%
 159 gelatin phantoms and fitted curves of the Kelvin–Voigt model for Scholte waves. For gelatin phantoms,
 160 the averaged data for 4 samples are presented as solid curves, and the standard deviation is presented
 161 as shaded areas.

162
 163 Figure 3C shows the speed-frequency relationship for various flat phantoms: 2% agarose, 10% gelatin
 164 and 15% gelatin. Two propagation regimes were observed: low frequencies (transient regime)
 165 exhibited large variations due to the increase in speed, starting from almost 0, and normal modes,
 166 related to the dimensions of the medium. At wavelengths close to half the medium thickness (below
 167 1.5 kHz for agarose and below 0.4 kHz for gelatin), waves became boundary-sensitive. Beyond these
 168 frequencies, dispersion stabilized, indicating a viscoelastic regime. These observations aligned with the
 169 findings of Laloy-Borgna et al.³³ for thin gelatin phantoms, where shear, Rayleigh, or Scholte waves
 170 propagates, and a viscoelastic rheological model could be applied. At higher frequencies, fluctuations
 171 are observed. They could possibly be explained by normal modes, or by a low signal to noise ratio in
 172 the measurement. Modeling the elastic moduli of different phantoms involved fitting a Kelvin–Voigt

173 model (Eq. 7) adapted to Scholte waves in the viscoelastic regime while disregarding normal modes
174 above 3 kHz for agarose and 2 kHz for gelatin. Quantitative results, along with data from the literature,
175 are displayed in Table 1^{31,34}.

176

177

178

179

180

181

182

183

184

185

Sample	Frequency range (kHz)	μ_1 (kPa)	μ_2 (Pa.s)
2% Agarose	1.5–3.0	156	1.49
10% Gelatin 10% (N = 4)	0.4–2.0	10.5 ± 3.25	0.75 ± 0.12
15% Gelatin (N = 4)	0.4–2.0	21.2 ± 0.63	1.27 ± 0.56
10% Gelatin ³⁴	0.1–0.6	5.34 ± 0.48	0.13 ± 0.50
15% Gelatin ³⁴	0.1–0.6	8.40 ± 0.59	1.22 ± 0.78
2% Agar – 3% gelatin ³¹	0.1–0.5	5.67 ± 0.02	0.22 ± 0.01

186

Table 1: Elasticity measured in flat phantoms and comparison with results from the literature

187

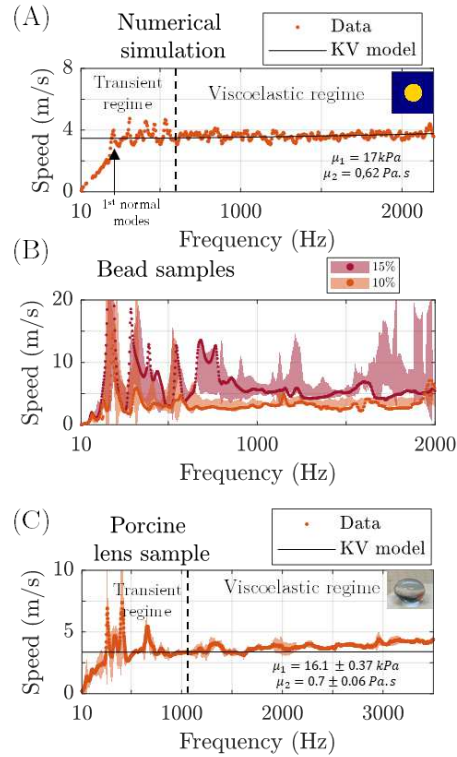
188

189

190

191

These results build upon previous studies that validated the assessment of phantom elasticity through surface wave tracking^{32,35,36}. To improve the representation of the lens geometry and size, numerical simulations of homogeneous inclusions and gelatin bead experimental models were developed. Figure 4 presents the results for these models and compares them to *in vitro* studies of porcine lenses.



192

193 FIG. 4. (A): Numerical simulation of a cylindrical inclusion (yellow) with $c_T=4$ m/s and $\mu_1=0.6$ Pa.s,
 194 surrounded by a medium (blue) with $c_T \approx 0$ m/s. Simulated data (dotted orange curve) and the adapted
 195 Kelvin–Voigt model (solid black) are shown. Quantitative values of μ_1 and μ_2 resulting from fitting the
 196 model are displayed in the lower right corner. (B) Experimental results in 10% and 15% gelatin beads.
 197 The results for each concentration (orange dotted curve for 10%, red dotted curve for 15%) and the
 198 standard deviations for 4 samples (shaded areas) are presented. (C): Experimental results for porcine
 199 lens samples. Averages of data for 3 repeated measurements (dotted curve), standard deviation
 200 (shaded area) and the model (solid black line) are shown. μ_1 and μ_2 resulting from fitting the model
 201 are displayed in the lower right corner.

202

203 A simulation of a cylindrical inclusion exhibits a dispersion curve similar to the findings for a flat
 204 phantom. At low frequencies, a speed increase indicated a guided wave regime, and the presence of
 205 peaks indicated a transient regime, likely attributed to the occurrence of normal mode at these
 frequencies. Theoretical predictions suggest that the first normal mode in a free disc should occur

206 around 300 Hz³⁷. However, due to the viscoelastic nature and immersion of the disc, this first
207 resonance shifts to a lower frequency (approximately 250 Hz), as indicated by the black arrow in Figure
208 4A. The variations are less important at high frequencies due to the viscosity attenuation. As the
209 frequency increased, the velocity stabilized toward the initial simulation parameters, indicating a
210 viscoelastic regime where the wavelength was smaller than the diameter of the inclusion. Fitting a
211 Kelvin–Voigt model yielded quantitative values ($\mu_1 = 17.0 \text{ kPa}$, $c_T = 4.12 \text{ m/s}$, $\mu_2 = 0.62 \text{ Pa}\cdot\text{s}$)
212 close to the simulation parameters. Figure 4B shows the results obtained from gelatin beads. A single
213 representative example is displayed for each concentration, along with the standard deviation
214 calculated from the four samples. The speed decreases at low frequencies, indicative of guided waves
215 regime, can be observed. The bead's curves exhibit several peaks and significant variations among
216 samples of the same concentration, attributed to experimental variables such as inhomogeneity in the
217 gelatin mixture, imperfect molding, and imperfect mechanical coupling between the bead and the
218 sample holder. Following the same protocol used for the crystalline lens (embedding the sample inside
219 the holder) was impossible because of gelatin bead melting by the hot agarose mixture. Additionally,
220 some peaks might be explained by the presence of structural resonances around the bead, such as in
221 the sample holder. Precisely explaining all the peaks and simulating the bead's configuration is difficult
222 and outside the scope of this experiment that aims at measuring a difference in speed between the
223 two concentrations. Figure 4C demonstrates curvilinear elastography applied to a single porcine lens
224 sample, with three repeated measurements. Dispersion curves similar to those in previous
225 experiments were observed. Our interpretation suggests the presence of normal modes and guided
226 wave dispersion in the lower frequency range (0.01-1.3 kHz), while the speed was more stable in the
227 range of 1.3–3.5 kHz. Comparisons could be made to flat phantoms and simulation results, with the
228 first range corresponding to guided waves and the second to Scholte wave dispersion. Fewer normal
229 modes were observed for the lens than the gelatin beads, likely due to the inherent asymmetry
230 between the anterior and posterior radii of curvature of the lens. Based on these observations and
231 using the Kelvin–Voigt model (Eq. 7) adapted to Scholte conditions, the dispersion curve was fit in the
232 1.3-3.0 kHz range, assuming that the observed dispersion was solely due to viscosity. The average shear
233 elasticity modulus for 11 lens samples was $20.5 \pm 6.40 \text{ kPa}$, and the average shear viscosity modulus
234 was $0.81 \pm 0.40 \text{ Pa}\cdot\text{s}$.

235 Our spectrometric approach, inspired by noise correlation algorithms, enabled surface wave speed
236 evaluation in the 0.1-3.5 kHz range for various models: flat gelatin phantoms, gelatin beads, a
237 numerical inclusion (2D) and porcine lens samples. It provided valuable insights into the viscoelasticity
238 of certain models, such as flat gelatin phantoms, numerical inclusions, and porcine lenses. Due to the
239 complexity and multitude of normal modes, the method could not accurately determine viscoelasticity

240 values of the gelatin beads. Nevertheless, the method confirmed the presence of guided waves in the
241 low-frequency range, which was consistent with observations of thin gelatin plates and simulations. In
242 the viscoelastic regime, where waves were not influenced by the boundaries of the medium, a Kelvin-
243 Voigt model was fitted, and the results were consistent with the literature (Table 1). Input viscoelastic
244 parameters were retrieved from numerical simulations. Based on these findings and the similar shapes
245 of the dispersion curves in the lens samples, quantitative values of viscoelasticity were computed
246 within the viscoelastic regime. The average elasticity was 20.5 ± 6.4 kPa, and the viscosity was 0.81 ± 0.40
247 Pa.s. The results from the literature were converted to the shear elasticity modulus, μ_1 , assuming
248 incompressibility ($\mu_1 = E/3$, where E is Young's modulus). The shear viscosity moduli in the samples
249 from the youngest subjects were slightly larger than those reported by Zhang et al.²³ at 0.55 ± 0.04
250 Pa.s. The average shear elasticity moduli for lens samples in our study were larger than those reported
251 in the literature. However, comparisons were challenging due to various uncontrolled parameters,
252 such as animal models, measurement protocols, frequency range, and temperature. Static methods
253 such as the microindentation method measured shear moduli of 0.2–0.7 kPa for young porcine lens
254 samples cut in half^{9,10}. The method, which was based on displacements of local bubbles by ARFI,
255 measured shear moduli of 0.4–2 kPa (gradient from the center to the cortex of young porcine lenses)^{15–}
256 ¹⁷. Dynamic methods measuring elastic wave velocities found typical shear moduli of 2–3 kPa for the
257 young porcine model^{20–23}. These studies assumed the propagation of surface waves such as Rayleigh
258 or Scholte waves regardless of the studied frequency. This highlighted that reporting the excitation
259 frequency is crucial for estimating viscoelastic properties. In our study, we described the wave
260 dispersion in the lens and observed guided waves propagating at low frequencies, which resulted in
261 decreases in velocity and apparent elasticity moduli. This suggested that methods relying on guided
262 waves (low frequency) may be biased. Specifically, in the viscoelastic study by Zhang et al.²³, the
263 dispersion curves did not exhibit the two regimes observed in our study, possibly due to the frequency
264 spread of the ARFI excitation signal, which can smooth results over a frequency range. The hardness
265 of the capsule (~ 1 MPa)^{38,39} may impact measurements, and the influence of the membrane on
266 elasticity measurements must be further studied. Additionally, to confirm the hypothesis that
267 dispersion in the viscoelastic regime is solely due to viscosity, the influence of an elasticity gradient on
268 speed measurement must be considered. Our method offers fast measurements (500 ms) over a broad
269 frequency range, while other studies, especially those using OCT imaging, require repeated and
270 synchronized excitations for each A-mode of the image^{18,20–23}. A limitation of our study was the need
271 to excise the lens from the eye and embed it in a gel for optimal mechanical coupling. Working at
272 frequencies above the transient regime is crucial for accurate quantitative characterization, requiring
273 high-frequency transmission to the lens in situ. Alternative excitation methods, such as ARFI or bubble-
274 induced tissue motion, may be more suitable than a mechanical vibrator. However, working at low

275 frequencies in the transient regime may enable the use of pulsatile blood flow and provide a
276 noninvasive approach.

277 In conclusion, our *in vitro* study demonstrated the application of the harmonic analysis of
278 surface waves propagating on a crystalline lens to assess viscoelastic parameters of porcine lenses.
279 Higher frequencies (>1 kHz) were crucial to prevent dispersion from guided waves and derive
280 quantitative values of elasticity. Elastic moduli of porcine lenses were larger than those reported in the
281 literature. Future research should focus on differentiating between lenses of various ages to detect
282 presbyopia and developing noninvasive protocols for data collection.

283

284 AUTHORS' CONTRIBUTIONS

285 AG wrote the versions of the manuscript that were subsequently edited by SC, ML, and FL. AG,
286 FL, SC and ML designed the experimental plan. AG performed the experiments and processed the
287 experimental data. GLB, AG and FL developed the method for data analysis. FL performed the
288 simulations. OBM, FM and SP collected the biological samples. GT, PG, CL, ML and SC provided the
289 project administration and funding.

290

291 ACKNOWLEDGMENTS

292 This work was partly supported by grant number ANR -21-CE19-0059-02.

293

294 AIP PUBLISHING DATA SHARING POLICY

295 The data that support the findings of this study are available from the corresponding author
296 upon reasonable request.

297

298

299 ¹ K.R. Heys, S.L. Cram, and R.J.W. Truscott, "Massive increase in the stiffness of the human lens
300 nucleus with age: the basis for presbyopia?", *Mol. Vis.*, **10** (n.d.).

301 ² R.F. Fisher, "The elastic constants of the human lens," *J. Physiol.* **212**(1), 147–180 (1971).

302 ³ T.R. Fricke, N. Tahhan, S. Resnikoff, E. Papas, A. Burnett, S.M. Ho, T. Naduvilath, and K.S. Naidoo,
303 "Global Prevalence of Presbyopia and Vision Impairment from Uncorrected Presbyopia,"
304 *Ophthalmology* **125**(10), 1492–1499 (2018).

305 ⁴ S.A. Strenk, L.M. Strenk, and J.F. Koretz, "The mechanism of presbyopia," *Prog. Retin. Eye Res.*
306 **24**(3), 379–393 (2005).

307 ⁵ G.S. Wilde, H.J. Burd, and S.J. Judge, "Shear modulus data for the human lens determined from a
308 spinning lens test," *Exp. Eye Res.* **97**(1), 36–48 (2012).

309 ⁶ A. Glasser, and M. C.W. Campbell, "Biometric, optical and physical changes in the isolated human
310 crystalline lens with age in relation to presbyopia," *Vision Res.* **39**(11), 1991–2015 (1999).

311 ⁷ H.A. Weeber, G. Eckert, F. Soergel, C.H. Meyer, W. Pechhold, and R.G.L. van der Heijde, "Dynamic
312 mechanical properties of human lenses," *Exp. Eye Res.* **80**(3), 425–434 (2005).

313 ⁸ P.K. Sharma, H.J. Busscher, T. Terwee, S.A. Koopmans, and T.G. van Kooten, "A comparative study
314 on the viscoelastic properties of human and animal lenses," *Exp. Eye Res.* **93**(5), 681–688 (2011).

315 ⁹ H.A. Weeber, G. Eckert, W. Pechhold, and R.G.L. van der Heijde, "Stiffness gradient in the crystalline
316 lens," *Graefes Arch. Clin. Exp. Ophthalmol.* **245**(9), 1357–1366 (2007).
317 ¹⁰ M.A. Reilly, and V.N. Ravi, "Microindentation of the young porcine ocular lens.," *J. Biomech. Eng.-*
318 *Trans. Asme* **131**(4), 044502–044502 (2009).
319 ¹¹ S. Besner, G. Scarcelli, R. Pineda, and S.-H. Yun, "In Vivo Brillouin Analysis of the Aging Crystalline
320 Lens," *Investig. Ophthalmology Vis. Sci.* **57**(13), 5093 (2016).
321 ¹² G. Scarcelli, P. Kim, and S.H. Yun, "In Vivo Measurement of Age-Related Stiffening in the Crystalline
322 Lens by Brillouin Optical Microscopy," *Biophys. J.* **101**(6), 1539–1545 (2011).
323 ¹³ S. Reiß, G.K.G. Burau, O. Stachs, R.F. Guthoff, and H. Stolz, "Spatially resolved Brillouin
324 spectroscopy to determine the rheological properties of the eye lens," *Biomed. Opt. Express* **2**(8),
325 2144–2159 (2011).
326 ¹⁴ G. Scarcelli, W.J. Polacheck, H.T. Nia, K. Patel, A.J. Grodzinsky, R.D. Kamm, and S.H. Yun,
327 "Noncontact three-dimensional mapping of intracellular hydromechanical properties by Brillouin
328 microscopy," *Nat. Methods* **12**(12), 1132–1134 (2015).
329 ¹⁵ S. Yoon, S. Aglyamov, A. Karpiouk, and S. Emelianov, "The Mechanical Properties of Ex Vivo Bovine
330 and Porcine Crystalline Lenses: Age-Related Changes and Location-Dependent Variations,"
331 *Ultrasound Med. Biol.* **39**(6), 1120–1127 (2013).
332 ¹⁶ T.N. Erpelding, K.W. Hollman, and M. O'Donnell, "Mapping age-related elasticity changes in
333 porcine lenses using bubble-based acoustic radiation force," *Exp. Eye Res.* **84**(2), 332–341 (2007).
334 ¹⁷ K.W. Hollman, M. O'Donnell, and T.N. Erpelding, "Mapping elasticity in human lenses using bubble-
335 based acoustic radiation force," *Exp. Eye Res.* **85**(6), 890–893 (2007).
336 ¹⁸ X. Zhang, Q. Wang, Z. Lyu, X. Gao, P. Zhang, H. Lin, Y. Guo, T. Wang, S. Chen, and X. Chen,
337 "Noninvasive assessment of age-related stiffness of crystalline lenses in a rabbit model using
338 ultrasound elastography," *Biomed. Eng. OnLine* **17**(1), 75 (2018).
339 ¹⁹ C. Wu, Z. Han, S. Wang, J. Li, M. Singh, C. -h. Liu, S. Aglyamov, S. Emelianov, F. Manns, and K.V.
340 Larin, "Assessing Age-Related Changes in the Biomechanical Properties of Rabbit Lens Using a
341 Coaligned Ultrasound and Optical Coherence Elastography System," *Invest. Ophthalmol. Vis. Sci.*
342 **56**(2), 1292–1300 (2015).
343 ²⁰ Y. Li, J. Zhu, J.J. Chen, J. Yu, Z. Jin, Y. Miao, A.W. Browne, Q. Zhou, and Z. Chen, "Simultaneously
344 imaging and quantifying *in vivo* mechanical properties of crystalline lens and cornea using optical
345 coherence elastography with acoustic radiation force excitation," *APL Photonics* **4**(10), 106104
346 (2019).
347 ²¹ H. Zhang, C. Wu, M. Singh, A. Nair, S.R. Aglyamov, and K.V. Larin, "Optical coherence elastography
348 of cold cataract in porcine lens," *J. Biomed. Opt.* **24**(03), 1 (2019).
349 ²² Y. Chen, S. Ye, Q. Wang, M. Shen, F. Lu, J. Qu, and D. Zhu, "In situ assessment of lens elasticity with
350 noncontact optical coherence elastography," *Biomed. Opt. Express* **13**(12), 6671 (2022).
351 ²³ H. Zhang, M. Singh, F. Zvietcovich, K. Larin, and S. Aglyamov, "Age-related changes in the
352 viscoelasticity of rabbit lens characterised by surface wave dispersion analysis," *Quantum Electron.*
353 **52**(1), 42–47 (2022).
354 ²⁴ M. Capriotti, J.F. Greenleaf, and M.W. Urban, "Time-Aligned Plane Wave Compounding Methods
355 for High-Frame-Rate Shear Wave Elastography: Experimental Validation and Performance
356 Assessment on Tissue Phantoms," *Ultrasound Med. Biol.* **47**(7), 1931–1948 (2021).
357 ²⁵ I. Sanchez, R. Martin, F. Ussa, and I. Fernandez-Bueno, "The parameters of the porcine eyeball,"
358 *Graefes Arch. Clin. Exp. Ophthalmol.* **249**(4), 475–482 (2011).
359 ²⁶ G.F. Pinton, J.J. Dahl, and G.E. Trahey, "Rapid tracking of small displacements with ultrasound,"
360 *IEEE Trans. Ultrason. Ferroelectr. Freq. Control* **53**(6), 1103–1117 (2006).
361 ²⁷ S. Catheline, R. Souchon, M. Rupin, J. Brum, A.H. Dinh, and J.-Y. Chapelon, "Tomography from
362 diffuse waves: Passive shear wave imaging using low frame rate scanners," *Appl. Phys. Lett.* **103**(1),
363 014101 (2013).
364 ²⁸ T.-M. Nguyen, A. Zorghi, M. Lescanne, C. Boccara, M. Fink, and S. Catheline, "Diffuse shear wave
365 imaging: toward passive elastography using low-frame rate spectral-domain optical coherence
366 tomography," *J. Biomed. Opt.* **21**(12), 126013 (2016).

367 ²⁹ A. Marmin, G. Laloy-Borgna, S. Facca, S. Gioux, S. Catheline, and A. Nahas, "Time-of-flight and
368 noise-correlation-inspired algorithms for full-field shear-wave elastography using digital holography,"
369 J. Biomed. Opt. **26**(08), (2021).

370 ³⁰ T.L. Szabo, in *Diagn. Ultrasound Imaging Second Ed.*, edited by T.L. Szabo, Second Edition
371 (Academic Press, Boston, 2014), pp. 81–119.

372 ³¹ S. Catheline, J.-L. Gennisson, G. Delon, M. Fink, R. Sinkus, S. Abouelkaram, and J. Culioli,
373 "Measurement of viscoelastic properties of homogeneous soft solid using transient elastography: An
374 inverse problem approach," J. Acoust. Soc. Am. **116**(6), 3734–3741 (2004).

375 ³² I.Z. Nenadic, M.W. Urban, M. Bernal, and J.F. Greenleaf, "Phase velocities and attenuations of
376 shear, Lamb, and Rayleigh waves in plate-like tissues submerged in a fluid (L)," J. Acoust. Soc. Am.
377 **130**(6), 3549–3552 (2011).

378 ³³ G. Laloy-Borgna, A. Zorgani, and S. Catheline, "Micro-elastography: Toward ultrasonic shear waves
379 in soft solids," Appl. Phys. Lett. **118**(11), 113701 (2021).

380 ³⁴ X. Zhang, B. Qiang, and J. Greenleaf, "Comparison of the surface wave method and the indentation
381 method for measuring the elasticity of gelatin phantoms of different concentrations," Ultrasonics
382 **51**(2), 157–164 (2011).

383 ³⁵ Royer, and Valier-Brasier, in *Elastic Waves Solids*, John Wiley&Sons (2022).

384 ³⁶ J. Liu, J. Leer, S.R. Aglyamov, and S.Y. Emelianov, "A Scholte wave approach for ultrasonic surface
385 acoustic wave elastography," Med. Phys., mp.16394 (2023).

386 ³⁷ A.C. Eringen, and E.S. Şuhubi, *Elastodynamics* (Academic press, NY San Francisco London, 1975).

387 ³⁸ K.S. Avetisov, N.A. Bakhchieva, S.E. Avetisov, I.A. Novikov, A.A. Frolova, A.A. Akovantseva, Yu.M.
388 Efremov, S.L. Kotova, and P.S. Timashev, "Biomechanical properties of the lens capsule: A review," J.
389 Mech. Behav. Biomed. Mater. **103**, 103600 (2020).

390 ³⁹ T. Mekonnen, C. Zevallos-Delgado, H. Zhang, M. Singh, S.R. Aglyamov, and K.V. Larin, "The lens
391 capsule significantly affects the viscoelastic properties of the lens as quantified by optical coherence
392 elastography," Front. Bioeng. Biotechnol. **11**, 1134086 (2023).

393